

8. Li, X. *et al.* The predictability of the magnetosphere and space weather. *Eos* **84**, 361, 369–370 (2003).
9. Baker, D. N., Kanekal, S. G., Pulkkinen, T. I. & Blake, J. B. Equinoctial and solstitial averages of magnetospheric relativistic electrons: A strong semiannual modulation. *Geophys. Res. Lett.* **26**, 3193–3196 (1999).
10. Blake, J. B. *et al.* New high temporal and spatial resolution measurements by SAMPEX of the precipitation of relativistic electrons. *Adv. Space Res.* **18**, 171–177 (1996).
11. Looper, M. D. *et al.* Observations of remnants of the ultrarelativistic electrons injected by the strong SSC of 24 March 1991. *Geophys. Res. Lett.* **21**, 2079–2082 (1994).
12. Li, X. *et al.* Simulation of the prompt energization and transport of radiation particles during the March 23, 1991 SSC. *Geophys. Res. Lett.* **20**, 2423–2426 (1993).
13. Li, X. in *Proc. 6th Int. Conf. on Substorms (ICS6)* (ed. Winglee, R. M.) 305–311 (Univ. Washington Press, Seattle, Washington, 2000).
14. Carpenter, D. L. & Park, C. G. What ionospheric workers should know about the plasmapause/plasmasphere. *Rev. Geophys.* **11**, 133–154 (1973).
15. Grebowsky, J. M. Model study of plasmapause motion. *J. Geophys. Res.* **75**, 4329–4333 (1970).
16. Thorne, R. M., Smith, E. J., Burton, R. K. & Holzer, R. E. Plasmaspheric hiss. *J. Geophys. Res.* **78** (10), 1581–1598 (1973).
17. Lorentzen, K. R., Blake, J. B., Inan, U. S. & Bortnik, J. Observations of relativistic electron microbursts in association with VLF chorus. *J. Geophys. Res.* **A 106**, 6017–6027 (2001).
18. Burch, J. L. *et al.* Views of the Earth's magnetosphere with the IMAGE satellite. *Science* **291**, 619–624 (2001).
19. Sandel, B. R., Goldstein, J., Gallagher, D. L. & Spasojevic, M. Extreme ultraviolet imager observations of the structure and dynamics of the plasmasphere. *Space Sci. Rev.* **109**, 25–46 (2003).
20. Goldstein, J. *et al.* Simultaneous remote sensing and *in situ* observations of plasmaspheric drainage plumes. *J. Geophys. Res.* **109**, doi:10.1029/2003JA010281 (2004).
21. Russell, C. T., Cartwright, M. & Kanekal, S. The formation of the inner zone trapped radiation belt. *Adv. Space Res.* (in the press).
22. Liu, W. W., Rostoker, G. & Baker, D. N. Internal acceleration of relativistic electrons by large-amplitude ULF pulsations. *J. Geophys. Res.* **104**, 17391–17407 (1999).
23. Summers, D., Thorne, R. M. & Xiao, F. Relativistic theory of wave-particle resonant diffusion with application to electron acceleration in the magnetosphere. *J. Geophys. Res.* **A 103**, 20487–20500 (1998).
24. Summers, D. & Thorne, R. M. Relativistic electron pitch-angle scattering by electromagnetic ion cyclotron waves during geomagnetic storms. *J. Geophys. Res.* **108**, doi:10.1029/2002JA009489 (2003).
25. Webb, D. F. & Allen, J. H. Spacecraft and ground anomalies related to the October–November 2003 solar activity. *Space Weather* **2**, doi:10.1029/2004SW000075 (2004).

Acknowledgements This work was supported by NASA. We thank members of the SAMPEX and IMAGE science teams for data and discussions.

Competing interests statement The authors declare that they have no competing financial interests.

Correspondence and requests for materials should be addressed to D.N.B. (daniel.baker@lasp.colorado.edu).

Hall-effect evolution across a heavy-fermion quantum critical point

S. Paschen¹, T. Lühmann¹, S. Wirth¹, P. Gegenwart¹, O. Trovarelli¹, C. Geibel¹, F. Steglich¹, P. Coleman² & Q. Si³

¹Max Planck Institute for Chemical Physics of Solids, Nöthnitzer Straße 40, D-01187 Dresden, Germany

²Center for Materials Theory, Department of Physics and Astronomy, Rutgers University, Piscataway, New Jersey 08855, USA

³Department of Physics and Astronomy, Rice University, Houston, Texas 77005-1892, USA

A quantum critical point (QCP) develops in a material at absolute zero when a new form of order smoothly emerges in its ground state. QCPs are of great current interest because of their singular ability to influence the finite temperature properties of materials. Recently, heavy-fermion metals have played a key role in the study of antiferromagnetic QCPs. To accommodate the heavy electrons, the Fermi surface of the heavy-fermion paramagnet is larger than that of an antiferromagnet^{1–3}. An important unsolved question is whether the Fermi surface transformation at the QCP develops gradually, as expected if the magnetism is of spin-density-wave (SDW) type^{4,5}, or suddenly, as expected if the heavy electrons are abruptly localized by magnetism^{6–8}. Here we report measurements of the low-temperature Hall coefficient

(R_H)—a measure of the Fermi surface volume—in the heavy-fermion metal YbRh_2Si_2 upon field-tuning it from an antiferromagnetic to a paramagnetic state. R_H undergoes an increasingly rapid change near the QCP as the temperature is lowered, extrapolating to a sudden jump in the zero temperature limit. We interpret these results in terms of a collapse of the large Fermi surface and of the heavy-fermion state itself precisely at the QCP.

The compound YbRh_2Si_2 investigated here appears to be one of the best suited heavy-fermion metals known in which to study the evolution of the Hall effect across a QCP. Magnetic susceptibility and specific heat indicate that this compound orders antiferromagnetically via a second-order phase transition at very low temperatures (Néel temperature $T_N = 70$ mK)⁹. The antiferromagnetic nature of the transition is supported by NMR data¹⁰. Neutron scattering experiments to directly detect the magnetic order are not available to date, presumably owing to the smallness of the ordered moment¹¹. T_N is continuously suppressed down to the lowest experimentally accessed temperatures by application of a small magnetic field B_c ($B_{1c} \approx 0.7$ T for a field along the magnetically hard c axis, $B_{2c} \approx 60$ mT for a field within the easy tetragonal plane)¹². In addition, isothermal magnetostriction measurements indicate that the transition remains of second order down to at least 15 mK (ref. 13). Although a change from second to first order at even lower temperatures can, of course, not be strictly ruled out, the non-Fermi liquid behaviour observed for three decades of temperature ($10 \text{ mK} < T < 10 \text{ K}$)¹² is best described within a quantum critical picture. The use of tiny fields permits one to reversibly access the QCP without the introduction of additional disorder and without altering the character of the underlying zero-field transition¹⁴. Moreover, unlike the case of several other heavy-fermion compounds¹⁵ (and the high- T_c superconductors), the QCP is not hidden by superconductivity. This is in spite of the high quality of the YbRh_2Si_2 single crystals investigated here (residual resistivities of $\sim 1 \mu\Omega \text{ cm}$, ref. 12). The scaling analysis of the thermodynamic and dynamical properties (specific heat, magnetic susceptibility, electrical resistivity) suggests¹² that the field-induced QCP in YbRh_2Si_2 is of local^{6–8} rather than of itinerant^{4,5} type, similar to the doping-induced QCP in $\text{CeCu}_{6-x}\text{Au}_x$ (ref. 6). Hall-effect measurements may be used to access a static electronic property, namely the Fermi surface volume, for which clear-cut theoretical predictions exist for different types of QCP^{7,8,16}. The study presented here is, to our knowledge, the first systematic Hall-effect measurement at a heavy-fermion QCP.

The Hall effect, usually a rather complex quantity, appears to be surprisingly simple here, both in vanishingly small and in finite magnetic fields. Outside the quantum critical region, the Hall resistivity is linear in field, resembling the behaviour of simple metals. Furthermore, our analysis of the temperature-dependent Hall coefficient in terms of the anomalous Hall effect (Fig. 1a, Methods, and refs 17 and 18) reveals that the low-temperature (below about 1 K) Hall coefficient is dominated by its normal contribution. These features imply that the low-temperature Hall coefficient can be used, to a good approximation, as a measure of the Fermi surface volume. In the absence of photoemission and de Haas–van Alphen studies (the latter presumably never being available because of the very low critical magnetic field), and of electronic bandstructure calculations, this is, so far, the only information on the Fermi surface volume of YbRh_2Si_2 . At zero magnetic field, the data measured at the lowest temperatures tend to saturate at the value of the normal Hall coefficient extracted from the data between 7 K and room temperature (Fig. 1a). This indicates that, at $B = 0$, the Fermi surface volume is the same at the lowest temperatures as it is at high temperatures. Thus, even though there is evidence for the onset of Kondo screening at approximately 20 K (refs 9 and 12) and for surprisingly large effective quasiparticle masses in the antiferromagnetically ordered state close to the QCP¹², the local moments do not, at the lowest temperatures and at $B = 0$

appear to be incorporated into the Fermi surface. In the static sense^{1–3}, YbRh₂Si₂ may, in its unconventional antiferromagnetic state at $B < B_0$, therefore not be classified as a ‘heavy-fermion’ metal.

In the intermediate temperature range, between approximately 70 mK and 7 K, there is an additional contribution ΔR_H which is not due to the anomalous Hall effect (Fig. 1a). In the main part of Fig. 1b we show that, between 0.7 and 5 K, the cotangent of the Hall

angle is linear in T^2 (while $\Delta\rho \propto T$), indicating that the longitudinal and transverse scattering rates are different¹⁹. This type of behaviour is well known in high- T_c copper oxides, where it has been taken as evidence for spin-charge separation¹⁹. Note, however, that for YbRh₂Si₂ the temperature range where this relation holds (inset of Fig. 1b), is narrower than that where the non-Fermi liquid (NFL) behaviour $\Delta\rho \propto T$ is observed (from 100 mK to almost 10 K, ref. 12), even if YbRh₂Si₂ is field-tuned to quantum criticality

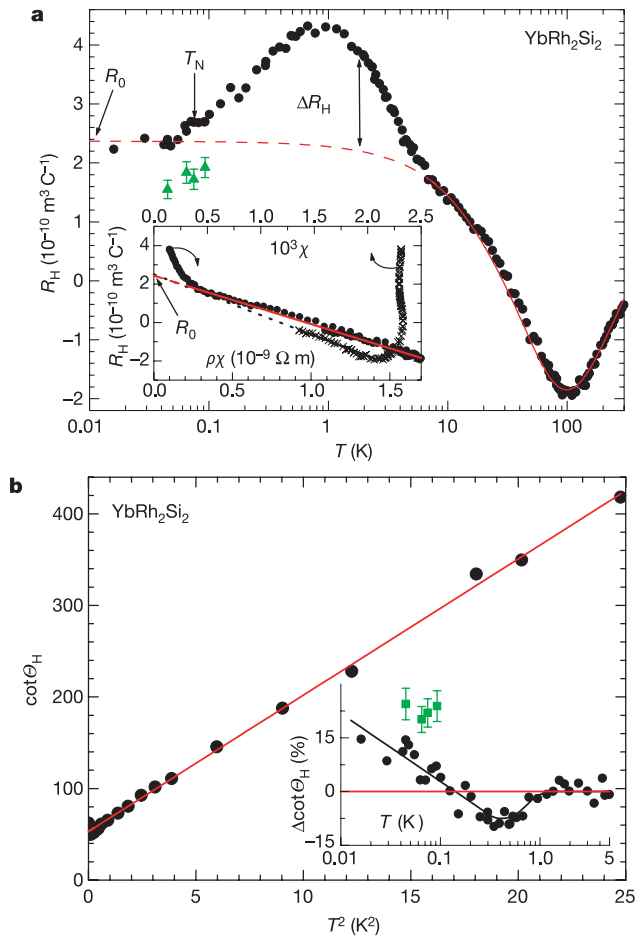


Figure 1 Temperature dependence of the Hall effect of YbRh₂Si₂. **a**, Temperature-dependent initial Hall coefficient $R_H(T)$, obtained from the initial slope of Hall resistivity versus field isotherms (Fig. 2a). The red curve corresponds to the red fit to the data from the inset. ΔR_H designates the difference between the data and the extrapolation of the fit. The green triangles correspond to R_H data obtained from the crossed-field experiment for large values of the tuning field B_2 (R_H^∞ values of fits to $R_H(B_2)$, see text and Fig. 2b), suggesting that the Fermi surface volume is distinctly larger in the field-induced paramagnetic state than in the antiferromagnetic state. Inset in **a**, initial Hall coefficient R_H versus product of electrical resistivity ρ and magnetic susceptibility χ (lower axis) and versus χ (upper axis), where temperature is an internal parameter. The full red (black) line is a linear fit according to the anomalous Hall-effect relation equation (3) (equation (5)) to the data between 7 and 300 K (90 and 300 K), the dashed lines are the extrapolations to $T = 0$. **b**, Cotangent of the Hall angle $\cot \theta_H (= \rho/(R_H B))$ as a function of T^2 , taken at $B = 1$ T. The red line (also in the inset) corresponds to a fit, $\cot \theta_H = C_1 + C_2 T^2$, where C_1 and C_2 are constants. Inset in **b**, difference between data and fit (red line) of main panel. The black line is a guide to the eye. Below 0.7 K, the data deviate considerably from the fit. The green squares correspond to $\cot \theta_H$ data obtained from the crossed-field experiment at the respective crossover fields ($B_2 = B_0$), indicating that, closer to the QCP, these deviations are even stronger. Thus, the $\cot \theta_H = C_1 + C_2 T^2$ behaviour appears to be a property of the regime at elevated temperatures where quantum critical fluctuations start to influence the physical properties, but it does not extend over the entire temperature region down to the QCP. Error bars, standard errors.

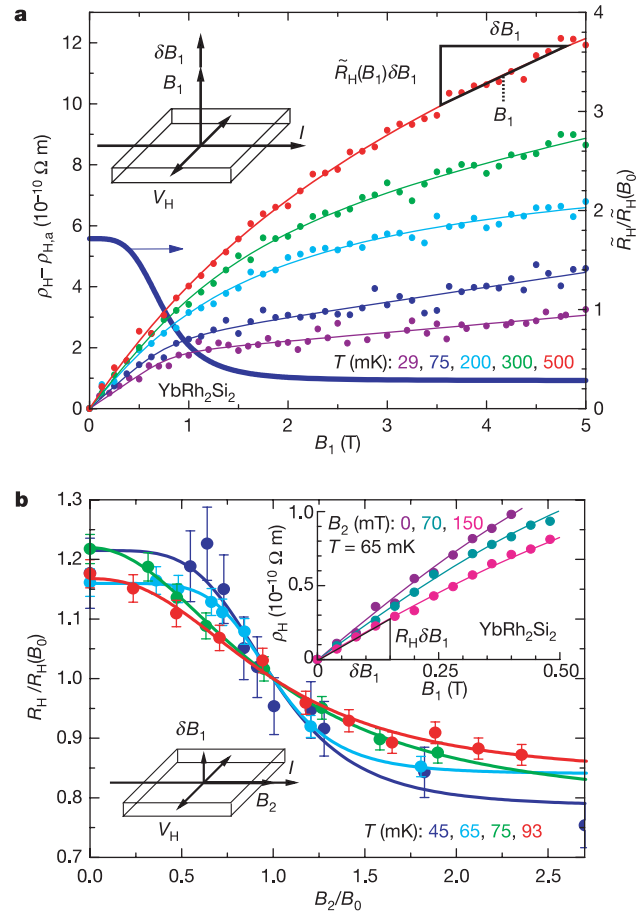


Figure 2 Magnetic field dependence of the Hall effect of YbRh₂Si₂. **a**, Single-field experiment. Typical isotherms of the Hall resistivity ρ_H , corrected for its anomalous contribution $\rho_{H,a}(B)$ (equation (6)), versus magnetic field $B_1 = \mu_0 H_1$ ($\parallel c$ -axis). The solid curves represent best fits, $\int \tilde{R}_H(B) dB$ (see text), to the data. The derivative of the fit at 75 mK is plotted on the right axis. **b**, Crossed-field experiment. Initial slope R_H , normalized to its value at the crossover field B_0 , of all measured ρ_H versus B_1 curves as a function of B_2/B_0 , at 45, 65, 75 and 93 mK. The solid lines represent best fits (see text) to the data. R_H decreases by a factor of ~ 1.5 upon going from the zero-field antiferromagnetic state to the field-induced paramagnetic state. In a spin-density-wave (SDW) picture, R_H is expected to evolve as the magnetic order parameter⁷. In YbRh₂Si₂, the ordered moment at $B = 0$ was estimated to be $\sim 0.002 \mu_B$ per Yb (ref. 11). Thus, the change in R_H corresponds to a factor of $\sim 750 \mu_B^{-1}$. The corresponding change of R_H by a factor of $\sim 30 \mu_B^{-1}$ observed for the SDW system Cr_{1-x}V_x (refs 22 and 26) was already considered a giant effect, possibly connected with bandstructure nesting effects³⁰. By comparison, the effect in YbRh₂Si₂ is about 25 times as large. Even in the absence of both experimental and theoretical studies of the electronic bandstructure of YbRh₂Si₂, we judge this effect far too large to be accounted for within an SDW picture. The same argument holds even if the second-order transition observed in the measured temperature range (> 15 mK) turned over into a first-order one at $T < 15$ mK. The inset in **b** displays ρ_H versus B_1 curves at three different values of the tuning field $B_2 = \mu_0 H_2$ ($\perp c$ -axis) at 65 mK. The solid lines represent best fits, as in **a**. Similar data have been obtained at the other temperatures (not shown). The sketches in **a** and **b** illustrate the experimental set-up. Error bars, standard errors.

(green squares in inset). The same may hold true for CeCoIn₅ (ref. 20).

In our field-dependent Hall-effect measurements on YbRh₂Si₂, the magnetic field plays dual roles, as both a ‘tuning’ and a ‘probe’ field. On the one hand, the coupling between the field and the Yb³⁺ moments tends to align the latter: it is this Zeeman-like coupling that tunes the ground state of the material, ultimately suppressing the antiferromagnetism and creating the QCP. On the other hand, the magnetic field also generates a weak Lorentz force on the underlying electrons, which produces the Hall response. The weak orbital coupling responsible for the Lorentz force does not appreciably change the ground state, so that, to a good approximation, we can discuss the two couplings independently. The single crystals of YbRh₂Si₂ are thin platelets oriented along the *a*–*b* plane, and practical Hall-effect measurements require a current and Hall voltage lying in this plane. This allows for two distinct types of experiment, namely ‘transverse tuning’ where the tuning field *B*₁ is parallel to the *c* axis, perpendicular to the current, and ‘longitudinal tuning’ where the tuning field *B*₂ lies parallel to the current in the basal plane (compare schematics in Fig. 2a and b). The longitudinal field *B*₂ produces essentially no Hall response (see Supplementary Methods 1), and serves only to tune the state: a separate, crossed probe field δB_1 along the *c* axis is required to measure the Hall response. In this longitudinal (crossed-field) experiment, the Hall resistivity ρ_H is a direct measure of the field-tuned (linear-response) Hall coefficient $R_H(B_2)$:

$$R_H(B_2) \equiv \lim_{B_1 \rightarrow 0} \rho_H(B_2, B_1) / B_1 \quad (1)$$

In the transverse (single-field) case, on the other hand, the

magnetic field simultaneously tunes the state and probes the Hall response, and the differential Hall coefficient $\tilde{R}_H(B_1)$ is:

$$\begin{aligned} \tilde{R}_H(B_1) &= \frac{d\rho_H(B_1)}{dB_1} = \left[\frac{\partial \rho_H(B_1)}{\partial B_1} \right]_{\text{orb}} + \left[\frac{\partial \rho_H(B_1)}{\partial B_1} \right]_{\text{zeeman}} \\ &= R_H(B_1) + \left[\frac{\partial \rho_H(B_1)}{\partial B_1} \right]_{\text{zeeman}} \end{aligned} \quad (2)$$

The orbital (‘probing’) contribution is, according to the Kubo formalism, just the generalized definition of a Hall coefficient (see Supplementary Methods 2). The Zeeman (‘tuning’) term is not related to a readily measurable linear-response quantity.

We first discuss the results of the single-field experiment. Figure 2a displays several representative isotherms of the Hall resistivity ρ_H , corrected for its anomalous contribution $\rho_{H,a}(B)$ (see Methods), versus *B*₁. $\rho_H - \rho_{H,a}$ shows a linear low-*B*₁ behaviour with larger slope, and a linear high-*B*₁ behaviour with smaller slope. The crossover between the two regimes broadens and shifts to higher *B*₁ with increasing temperature. For a quantitative analysis of the data we choose $\tilde{R}_H(B) = R_H^\infty - (R_H^\infty - R_H^0)\gamma(B)$ as a fitting function, where R_H^0 is the zero-field Hall coefficient and R_H^∞ is the asymptotic differential Hall coefficient at large fields. $\gamma(B)$ is a crossover function that changes from unity at low fields to zero at large fields, which we parameterize as $\gamma(B) = 1/[1 + (B/B_0)^p]$. Here, *B*₀ is the crossover field and *p* determines the sharpness of the transition, which has a width $\Gamma \approx B_0/p$ when *p* is large. For $p \rightarrow \infty$, $\int \tilde{R}_H(B)dB$ has a sharp kink at *B* = *B*₀, corresponding to a step in

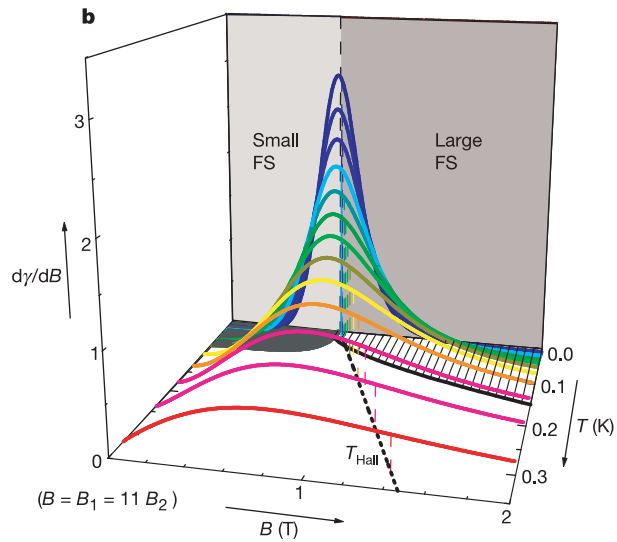
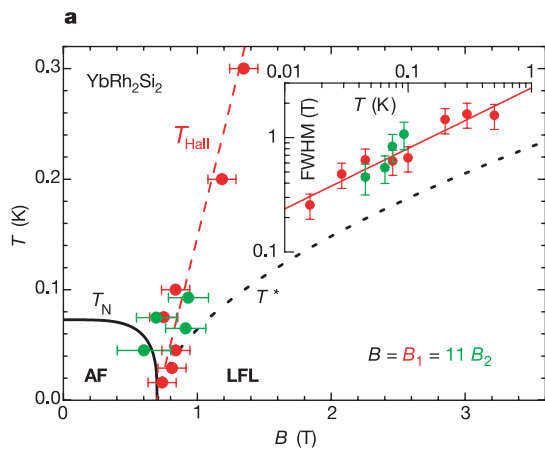


Figure 3 Temperature–field phase diagrams of YbRh₂Si₂. **a**, The red data points correspond to the *B*₀ values (crossover positions in the Hall-effect measurements) determined from the fits to the data in Fig. 2a (single-field experiment). Note that the horizontal bars represent the error in the determination of *B*₀ rather than the width of the crossover. The red dotted line denoted *T*_{Hall} is the best linear fit to all data up to 0.5 K. It extrapolates at zero temperature to ~ 0.7 T, the critical field *B*_{1c} for the direction parallel to the *c*-axis. The green data points correspond to 11*B*₀ determined from the fits to the data in Fig. 2b (crossed-field experiment). The full and dotted black curves represent the field dependence of the Néel temperature *T*_N and the crossover temperature *T*^{*} to a $\Delta\rho \propto T^2$ law, respectively, as determined from iso-field $\rho(T)$ data¹². The latter differs qualitatively from the cross-over line determined from a scaling analysis of both specific heat and resistivity data, yielding $T_{\text{cross}} \propto (B - B_c)$ (ref. 14). The inset shows the full-width at half-maximum (FWHM) of $d\tilde{R}_H(B_1)/dB_1$ in a log–log plot (red points). The red

solid line, $\propto T^a$, $a = 0.5 \pm 0.1$, is a best fit to these data. As in the main panel, the green dots correspond to the crossed-field experiment. For both the main panel and the inset, the red and green data points agree within the error bars. **b**, Three-dimensional representation of the field derivative of the crossover function $\gamma(B)$ defined in the text. The coloured curves represent arbitrary isotherms of $d\gamma(B)/dB$, obtained using both the *B*₀(*T*) fit of **a** and a power law fit to the corresponding $\rho(T)$ data (not shown). The field *B* corresponds to *B*₁||*c* or to 11*B*₂ ⊥ *c*. The positions *B*₀ are designated by broken drop lines and the black dotted line denoted *T*_{Hall} in the *T*–*B* plane. The antiferromagnetic (AF) phase and the region where $\Delta\rho \propto T^2$ (LFL) are marked as black and hatched areas, respectively, in the *T*–*B* plane. At the lowest temperatures, $d\gamma(B)/dB$ may be interpreted as indicating the change of the effective carrier concentration. In the limit $T \rightarrow 0$, $d\gamma(B)/dB$ is a δ -function (dotted line in the *T* = 0 plane), separating the states of small and large Fermi surface (FS) at *B* = *B*_{1c} = 11*B*_{2c}. Error bars, standard errors.

$\tilde{R}_H(B)$ itself. The fits to the data are shown as solid lines in Fig. 2a. For one temperature the derivative of the fit, corresponding to $\tilde{R}_H(B_1)$, is shown as well. The crossover fields B_0 obtained from these fits are included as red dots in the temperature–field (T – B) phase diagram of YbRh_2Si_2 (Fig. 3a). A linear fit to these points (dashed red line in Fig. 3a denoted T_{Hall}) extrapolates at zero temperature to the critical field $B_{1c} \approx 0.7$ T for the disappearance of antiferromagnetic order and the QCP. Thus, the crossover is directly related to the QCP. The sharpness of the crossover is best quantified by the full-width at half-maximum (FWHM) of $d\tilde{R}_H/dB_1$, which represents the change of slope of $\rho_H(B_1)$. The temperature dependence of the FWHM values is well described by a pure power law, $\text{FWHM} \propto T^a$, $a = 0.5 \pm 0.1$ (inset of Fig. 3a), suggesting that, at zero temperature, the crossover is infinitely sharp ($\text{FWHM} = 0$).

To understand the origin of this sharp feature, we now turn to the crossed-field measurement of the linear-response Hall coefficient, equation (1). The inset of Fig. 2b displays $\rho_H(B_1)$ curves taken at 65 mK for different values of the longitudinal tuning field B_2 . With increasing B_2 the linear-response Hall coefficient R_H decreases. For a quantitative analysis we fit, as above, $\int \tilde{R}_H(B)dB$ to the $\rho_H(B_1)$ data (solid lines in the inset of Fig. 2b). As opposed to the single-field experiment, $R_H^0 = R_H$ is now the only parameter to consider. R_H , normalized to its value at the crossover field B_0 , is plotted in the main panel of Fig. 2b as a function of the normalized tuning field B_2/B_0 . Data obtained in the same way at 45, 75 and 93 mK are included as well. R_H decreases as a function of B_2 by a factor of ~ 1.5 . In a simple one band model, this corresponds to an increase in the charge carrier concentration from ~ 2 to ~ 3 holes per YbRh_2Si_2 formula unit. The crossover sharpens up as the temperature is lowered. For a quantitative analysis, we may now fit the crossover form $R_H(B) = R_H^\infty - (R_H^\infty - R_H^0)\gamma(B)$ to the $R_H(B_2)$ data (solid curves in main panel of Fig. 2b). The R_H^∞ values obtained for these four temperatures are included as green triangles in the main part of Fig. 1a, showing that the Hall coefficient in the field-induced Landau Fermi liquid (LFL) state (compare Fig. 3a) at very low temperatures is substantially smaller than in the $B = 0$ antiferromagnetically ordered state. The $11B_0$ and FWHM values obtained from the above fits are included as green dots in Fig. 3a and its inset. The factor of 11 accounts for the fact that the tuning field B_2 is applied in the easy tetragonal plane of YbRh_2Si_2 where, owing to the magnetic anisotropy, the action of a magnetic field is known to be ~ 11 times as strong as along the magnetically hard c axis¹². For both quantities, the green and red data points agree within the error bars. Thus, the linear Hall response $R_H(B_2)$ of the crossed-field measurement and the differential Hall response $\tilde{R}_H(B_1)$ of the single-field measurement can be described by the same functional form, and the respective crossover positions and crossover widths agree quantitatively. This experimental finding suggests that the second term on the right hand side of equation (2) plays a minor role, at least in the experimentally accessed part of the T – B phase diagram. Therefore, here the single-field experiment appears to probe essentially the same (linear-response) Hall coefficient as the crossed-field experiment. However, there is a quantitative difference in the jump heights of $\tilde{R}_H(B_1)$ and $R_H(B_2)$, which probably reflects the anisotropies in the evolution of the electronic bandstructure under transverse and longitudinal field-tuning²¹, amplified by the likely presence of a multisheeted, anisotropic Fermi surface.

The phase diagram in the magnetic field–temperature parameter space can now be illustrated by a three-dimensional representation of $d\gamma(B)/dB$ (Fig. 3b). $\gamma(B)$ is calculated at arbitrary temperatures from the linear B_0 versus T fit (dashed red line in Fig. 3a) and a power law fit (not shown) to the $p(T)$ data obtained from the fits to $\rho_H(B_1)$ (Fig. 2a) and to $R_H(B_2)$ (main panel of Fig. 2b). With decreasing temperature, the $d\gamma(B)/dB$ curves sharpen up and their crossover position B_0 , designated by drop lines, shifts to lower fields such that, at zero temperature, a δ -function (dashed line in the

$T = 0$ plane in Fig. 3b) is situated at the QCP.

Thus, the extrapolation of our finite temperature data to zero temperature indicates the presence of a finite discontinuity ('jump') in the Hall coefficient at the QCP, even though the change in the magnetic order parameter is infinitesimal¹¹. By contrast, in an itinerant SDW scenario, the Fermi surface is expected⁷ to fold over at the QCP; the Hall coefficient is then continuous across the QCP, evolving gradually with the size of the antiferromagnetic order parameter, as is indeed observed experimentally²². (For a more quantitative comparison, see Fig. 2b legend). Our results hint at a sudden reconstruction of the Fermi surface at the QCP, corresponding to the sudden loss of 'mobile' $4f$ electrons^{7,8,16}. Loosely speaking, the volume of the Fermi surface has changed discontinuously. Here of course, the concept of Fermi surface volume needs to be treated with some care, for antiferromagnetism breaks translational symmetry. YbRh_2Si_2 may well be an easy-plane incommensurate antiferromagnet, and for this class of antiferromagnet, to linear order in the magnetic order parameter, the Fermi surface volume is well-defined in the paramagnetic unit cell. From our data we infer that the antiferromagnetic ground state has a 'small' Fermi surface, which is the same as the one extracted from the high-temperature Hall effect data (main panel of Fig. 1a), while the paramagnetic ground state has a 'large' Fermi surface, which presumably incorporates the new heavy-fermion states injected by the local moments.

The crossover line $T_{\text{Hall}}(B)$ (Fig. 3) is then interpreted as the finite temperature signature of the 'jump' in the Fermi surface volume. It delineates the position at which a new large Fermi surface emerges in the incoherent electron fluid. It is interesting that this precursor to heavy quasiparticle formation takes place at temperatures well above the temperature T^* (dashed black curve in Fig. 3a) below which the coherent LFL develops. The existence of a large Fermi surface in the absence of well-defined quasiparticles is well known in one-dimensional Luttinger liquids²³. It is also reminiscent of the marginal Fermi liquid behaviour in copper oxide superconductors, where a large Fermi surface is seen in the angle-resolved photoemission studies, but the scattering rate grows linearly, rather than quadratically, in temperature^{24,25}. Note also that the crossover line $T_{\text{Hall}}(B)$ does not follow the antiferromagnetic transition line $T_N(B)$ (Fig. 3a). Indeed, within experimental resolution, the initial Hall coefficient shows no change at the zero field Néel temperature of 70 mK (Fig. 1a). This behaviour contrasts markedly with that expected in an itinerant SDW, where changes in the Hall coefficient should coincide with the Néel transition—as is indeed observed for $\text{Cr}_{1-x}\text{V}_x$ (refs 22 and 26). Thus we may discard the possibility that the observed crossover in the Hall coefficient of YbRh_2Si_2 is due to a unit-cell doubling in a symmetry breaking antiferromagnetic transition.

Even though the crossover at $T_{\text{Hall}}(B)$ broadens rapidly with temperature (compare $\text{FWHM}(T)$ in the inset of Fig. 3a and width of $d\gamma(B)/dB$ in Fig. 3b), so that it can not be followed beyond about 0.5 K, the additional contribution ΔR_H to the initial Hall coefficient (main panel of Fig. 1a), which we attribute to fluctuations of the Fermi surface volume, can be discerned up to much higher temperatures of the order of 10 K. This is precisely the temperature below which NFL behaviour is observed in thermodynamic and dynamical properties^{9,12}. This observation makes it very tempting to hold fluctuations of the Fermi surface volume responsible for the NFL behaviour observed over this same temperature window. The fact that the NFL behaviour is observed in the entire phase diagram above T_N and T^* (and below 10 K) can be related to the broadness of the crossover. Interestingly, the spin fluctuation scale T_0 (extracted from a logarithmic fit $\Delta C_p/T \propto \ln(T_0/T)$ to the specific heat data for $0.3 \text{ K} < T < 10 \text{ K}$) and the single-ion Kondo temperature (which marks the onset of magnetic screening) extracted from a magnetic entropy measurement are of the same order of magnitude^{9,12}.

To summarize, we observe a rapid crossover of the Hall coefficient

as a function of a control parameter. By extrapolation to $T = 0$ of both the Hall crossover and the magnetic phase transition¹², we infer that a large jump of the Hall coefficient occurs at the QCP. We expect this new insight, made possible primarily by the absence of superconductivity, to have broad implications for other strongly correlated electron systems²⁷. □

Methods

Anomalous Hall effect

In general, the Hall effect of materials containing localized magnetic moments is dominated at high temperatures by an anomalous Hall effect produced by the left-right asymmetry in incoherent electron scattering processes²⁸. The initial or linear-response Hall coefficient R_H (Hall coefficient in zero-field limit) scales for many materials with the product of electrical resistivity ρ and magnetic susceptibility χ ,

$$R_H = R_0 + C\rho\chi \quad (3)$$

where R_0 is the normal Hall coefficient and C is a constant²⁸. The term $C\rho\chi$ represents the anomalous Hall effect due to intrinsic scattering. The temperature-independent extrinsic anomalous Hall coefficient R_{ex} due to skew scattering by residual defects may be estimated from

$$R_{ex} = C\rho_0\chi_0 \quad (4)$$

where ρ_0 is the residual resistivity and χ_0 the residual volume magnetic susceptibility²⁸. A model including crystalline electric field effects valid in the incoherent regime²⁹, on the other hand, predicts

$$R_H = R_0 + R_s\chi \quad (5)$$

instead of equation (3). Here R_s is a constant and $R_s\chi$ the anomalous Hall-effect term.

In Fig. 1a we have shown that also in YbRh₂Si₂ the high-temperature Hall coefficient is dominated by the anomalous Hall effect. Between 7 and 300 K (90 and 300 K), equation (3) (equation (5)) holds (compare inset of Fig. 1a). The R_0 value obtained for both models is $(2.4 \pm 0.1) \times 10^{-10} \text{ m}^3 \text{ C}^{-1}$, which corresponds, in a simple one band model, to a charge carrier concentration of $2.6 \times 10^{28} \text{ m}^{-3}$ (approximately 2 holes per formula unit of YbRh₂Si₂). Considering only the magnetic contribution to ρ in equation (3) yields similar values for R_0 (ref. 18). Below about 1 K, where the extrapolation of the fit according to equation (3) (red dashed curve in Fig. 1a) becomes temperature independent and saturates at the value of the normal Hall coefficient R_0 , the intrinsic anomalous Hall effect is negligible. The extrinsic anomalous Hall effect estimated from equation (4) with $\rho_0 \approx 1 \mu\Omega \text{ cm}$ and $\chi_0 = 0.0035 \text{ (B/C, } T = 40 \text{ mK)}$ (ref. 12) is less than 4% of R_0 and thus plays a negligible role. Therefore, below about 1 K, the initial Hall coefficient of YbRh₂Si₂ is essentially free of any anomalous contribution.

The anomalous Hall effect in finite magnetic fields may, in analogy with equation (3), be estimated from

$$\rho_{H,a}(B) = C\rho(B)\mu_0 M(B) \quad (6)$$

where $\rho(B)$ and $M(B)$ are the field-dependent electrical resistivity and magnetization, respectively.

For YbRh₂Si₂, $\rho(B)$ (not shown) and $M(B)$ (ref. 12) have been measured in the relevant geometry ($B \parallel c$, current $I \perp c$). For the parameter C we use the value extracted from the temperature dependence of the initial Hall coefficient (inset of Fig. 1a). $\rho_{H,a}$ is less than 20% of ρ_H at all temperatures and fields.

Received 1 July; accepted 14 October 2004; doi:10.1038/nature03129.

- Martin, R. M. Fermi-surface sum rule and its consequences for periodic Kondo and mixed-valence systems. *Phys. Rev. Lett.* **48**, 362–365 (1982).
- Fulde, P. in *Narrow-Band Phenomena—Influence of Electrons with both Band and Localized Character* (ed. Fuggle, J. C.) 27–29 (Plenum, New York, 1988).
- Oshikawa, M. Topological approach to Luttinger's theorem and Fermi surface of a Kondo lattice. *Phys. Rev. Lett.* **84**, 3370–3373 (2000).
- Hertz, J. A. Quantum critical phenomena. *Phys. Rev. B* **14**, 1165–1184 (1976).
- Millis, A. J. Effect of a nonzero temperature on quantum critical points in itinerant fermion systems. *Phys. Rev. B* **48**, 7183–7196 (1993).
- Schröder, A. et al. Onset of antiferromagnetism in heavy-fermion metals. *Nature* **407**, 351–355 (2000).
- Coleman, P., Pépin, C., Si, Q. & Ramazashvili, R. How do Fermi liquids get heavy and die? *J. Phys. Condens. Matter* **13**, R723–R738 (2001).
- Si, Q., Rabello, S., Ingersent, K. & Smith, J. L. Locally critical quantum phase transitions in strongly correlated metals. *Nature* **413**, 804–808 (2001).
- Trovarelli, O. et al. YbRh₂Si₂: Pronounced non-Fermi-liquid effects above a low-lying magnetic phase transition. *Phys. Rev. Lett.* **85**, 626–629 (2000).
- Ishida, K. et al. YbRh₂Si₂: Spin fluctuations in the vicinity of a quantum critical point at low magnetic fields. *Phys. Rev. Lett.* **89**, 107202 (2002).
- Ishida, K. et al. Low-temperature magnetic order and spin dynamics in YbRh₂Si₂. *Phys. Rev. B* **68**, 184401 (2003).
- Gegenwart, P. et al. Magnetic-field induced quantum critical point in YbRh₂Si₂. *Phys. Rev. Lett.* **89**, 056402 (2002).
- Küchler, R. et al. Low-temperature thermal expansion and magnetostriction of YbRh₂(Si_{1-x}Ge_x)₂ ($x = 0$ and 0.05). *J. Magn. Magn. Mater.* **272–276**, 229–230 (2004).
- Custers, J. et al. The break-up of heavy electrons at a quantum critical point. *Nature* **424**, 524–527 (2003).
- Stewart, G. R. Non-Fermi-liquid behavior in d - and f -electron metals. *Rev. Mod. Phys.* **73**, 797–855 (2001).

- Senthil, T., Vojta, M. & Sachdev, S. Weak magnetism and non-Fermi liquids near heavy-fermion critical points. *Phys. Rev. B* **69**, 035111 (2004).
- Paschen, S. et al. Hall effect of the NFL compound YbRh₂Si₂. *Acta Phys. Polon.* **B 34**, 359–362 (2003).
- Paschen, S. et al. Anomalous Hall effect in YbRh₂Si₂. *Physica B* (in the press).
- Anderson, P. W. Hall effect in the two-dimensional Luttinger liquid. *Phys. Rev. Lett.* **67**, 2092–2094 (1991).
- Nakajima, Y. et al. Normal-state Hall angle and magnetoresistance in quasi-2D heavy fermion CeCoIn₅ near a quantum critical point. *J. Phys. Soc. Jpn* **73**, 5–8 (2004).
- Custers, J. *Quantum-Critical Behavior in the Heavy-Fermion Compounds YbRh₂Si₂ and CeIn_{3-x}Sn_x*. PhD thesis, TU Dresden (2004).
- Lee, M., Husmann, A., Rosenbaum, T. F. & Aeppli, G. High resolution study of magnetic ordering at absolute zero. *Phys. Rev. Lett.* **92**, 187201 (2004).
- Haldane, F. D. M. 'Luttinger liquid theory' of one-dimensional quantum fluids: I. Properties of the Luttinger model and their extension to the general 1D interacting spinless Fermi gas. *J. Phys. C* **14**, 2585–2609 (1981).
- Varma, C. M., Littlewood, P. B., Schmitt-Rink, S., Abrahams, E. & Ruckenstein, A. E. Phenomenology of the normal state of Cu-O high-temperature superconductors. *Phys. Rev. Lett.* **63**, 1996–1999 (1989).
- Valla, T. et al. Evidence for quantum critical behaviour in the optimally doped cuprate Bi₂Sr₂CaCu₂O_{8+δ}. *Science* **285**, 2110–2113 (1999).
- Yeh, A. et al. Quantum phase transition in a common metal. *Nature* **419**, 459–462 (2002).
- Balakirev, F. F. et al. Signature of optimal doping in Hall-effect measurements on a high-temperature superconductor. *Nature* **424**, 912–915 (2003).
- Fert, A. & Levy, P. M. Theory of the Hall effect in heavy-fermion compounds. *Phys. Rev. B* **36**, 1907–1916 (1987).
- Kontani, H., Miyazawa, M. & Yamada, K. Theory of anomalous Hall effect in a heavy fermion system with a strong anisotropic crystal field. *J. Phys. Soc. Jpn* **66**, 2252–2255 (1997).
- Norman, M. R., Si, Q., Bazaliy, Y. B. & Ramazashvili, R. Hall effect in nested antiferromagnets near the quantum critical point. *Phys. Rev. Lett.* **90**, 116601 (2003).

Supplementary Information accompanies the paper on www.nature.com/nature.

Acknowledgements We acknowledge discussions with P. Bühler, J. Custers, C. Langhammer, C. Pépin, A. Rosch, A. Schofield, M. Vojta, A. Tselik and F. Weickert. Part of the work at Dresden was supported by the Fonds der Chemischen Industrie. P.C. and Q.S. are supported by the National Science Foundation. The work at Rice University was partially supported by the Welch Foundation and TCSAM.

Competing interests statement The authors declare that they have no competing financial interests.

Correspondence and requests for materials should be addressed to S.P. (paschen@cpfs.mpg.de).

Lensless imaging of magnetic nanostructures by X-ray spectro-holography

S. Eisebitt¹, J. Lüning², W. F. Schlotter^{2,3}, M. Lörger¹, O. Hellwig^{1,4}, W. Eberhardt¹ & J. Stöhr²

¹BESSY mbH, Albert-Einstein-Straße 15, 12489 Berlin, Germany

²SSL, Stanford Linear Accelerator Center, 2575 Sand Hill Road, Menlo Park, California 94025, USA

³Department of Applied Physics, 316 Via Pueblo Mall, Stanford University, Stanford, California 94305-4090, USA

⁴San Jose Research Center, Hitachi Global Storage Technologies, 650 Harry Road, San Jose, California 95120, USA

Our knowledge of the structure of matter is largely based on X-ray diffraction studies of periodic structures and the successful transformation (inversion) of the diffraction patterns into real-space atomic maps. But the determination of non-periodic nanoscale structures by X-rays is much more difficult. Inversion of the measured diffuse X-ray intensity patterns suffers from the intrinsic loss of phase information^{1,2}, and direct imaging methods are limited in resolution by the available X-ray optics³. Here we demonstrate a versatile technique for imaging nanostructures, based on the use of resonantly tuned soft X-rays for scattering contrast and the direct Fourier inversion of a holo-